

Web of Knowledge

Page 1 (Records 1 -- 1)

Close

Print

◀ [1] ▶

Record 1 of 1

Title: Vorticity visualization: Phantom study for a new discriminant parameter in US elastography - art. no. 65130K**Author(s):** Sosa-Cabrera, D (Sosa-Cabrera, D.); Rodriguez-Florida, MA (Rodriguez-Florida, M. A.); Suarez-Santana, E (Suarez-Santana, E.); Ruiz-Alzola, J (Ruiz-Alzola, Juan)**Editor(s):** Emelianov SY; McLeavey SA**Source:** Medical Imaging 2007: Ultrasonic Imaging and Signal Processing **Book Series:** PROCEEDINGS OF THE SOCIETY OF PHOTO-OPTICAL INSTRUMENTATION ENGINEERS (SPIE) **Volume:** 6513 **Pages:** K5130-K5130 **Article Number:** 65130K **DOI:** 10.1117/12.709251 **Published:** 2007**Accession Number:** WOS:000247373000018**Conference Title:** Medical Imaging 2007 Conference**Conference Date:** FEB 18-20, 2007**Conference Location:** San Diego, CA**Conference Sponsors:** SPIE, Amer Assoc Physicists, Amer Physiol Soc, Comp Assisted Radiol & Surg, Soc Imaging Sci & Technol, Med Image Percept Soc, Radiol Soc N Amer, Soc Imaging Informat Med, Soc Mole Imaging, DICOM Standards Comm**ISSN:** 0277-786X**ISBN:** 978-0-8194-6631-0

Web of Knowledge

Page 1 (Records 1 -- 1)

Close

Print

◀ [1] ▶

Documents

Sosa-Cabrera, D., Rodriguez-Florido, M.A., Suarez-Santana, E., Ruiz-Alzola, J.

Vorticity visualization: Phantom study for a new discriminant parameter in US elastography

(2007) *Progress in Biomedical Optics and Imaging - Proceedings of SPIE*, 6513, art. no. 65130K, . Cited 2 times.

Document Type: Conference Paper

Source: Scopus

About Scopus

[What is Scopus](#)

[Content coverage](#)

About Elsevier

[About Elsevier](#)

[Terms and Conditions](#)

[Privacy Policy](#)

Customer Service

[Contact and support](#)

[Live chat](#)



Copyright © 2013 Elsevier B.V. All rights reserved. Scopus® is a registered trademark of Elsevier B.V.

Vorticity Visualization: Phantom Study for a New Discriminant Parameter in US Elastography

D. Sosa-Cabrera ^a, M.A. Rodriguez-Florido ^{b,a} E. Suarez-Santana ^{b,a} and Juan Ruiz-Alzola ^{b,a}

^aCenter for Technology in Medicine, Dept. Señales y Comunicaciones,
University of Las Palmas de Gran Canaria, SPAIN;

^bCanary Islands Institute of Technology, SPAIN;

ABSTRACT

Ultrasound elastography measures the elastic properties of soft tissues using ultrasound signals. The elastic problem can be analyzed with tensor signal processing. In this work, we propose a new interpretation of elastography through the deformation tensor and its decomposition into both the strain and vorticity tensors. Vorticity gives information about the rotation of the inclusions that might help in the discrimination between malign and benign tumors without using biopsy. Although clinical validation is needed, synthetic experiments present reliable results.

1. INTRODUCTION

Much of the growth of cancer in the last 30 years was due to more people living longer - as cancer is a disease which usually affects older people. The causes of cancer are wide and varied, and its prevention is an extremely complex process that needs the development of new tools to help in the early detection and diagnosis of the disease.

Changes in tissue stiffness correlate with pathological phenomena that can aid the diagnosis of several diseases such as breast and prostate cancer ^{1,2} or cardiovascular dysfunctions.^{3,4} Many different approaches try to estimate and image the elastic properties of tissues, but this is not possible with conventional ultrasound, MRI, CT or nuclear imaging. There are mechanical ways to estimate the biomechanical properties of the tissue such as indentation, which is mostly used for thin layers of tissue *ex-vivo*.^{5,6}

Researchers have introduced new techniques using imaging modalities such as MRI and ultrasound, and also there are some investigations in the optical field using microscopes,⁷ always imaging the tissue response to some stimulus. A review is found in.⁸

Elastography⁹ relies among the ultrasound quasi-static techniques for imaging the elastic properties of soft tissues and it is well established in the literature. The standard mechanical way to produce a controlled compression in the tissue passes through a mechanical arm where the ultrasonic probe is held and used to compress within a plate, to make the stress field the more homogeneous as possible. However, in the last years, many researchers have focused on simplifying the elastographic set-up needed for the production of the stimulus to the tissue. There are studies comparing results¹⁰ which show that freehand elastography, although it has a lower SNR, has proven its capability to detect lesions such as breast carcinomas.¹¹

The displacement field from which researches normally obtain the strain is estimated with different techniques. We will refer to papers such as,¹² which use time-domain cross-correlation techniques, or,¹³ which uses iterative phase zero estimation, among others. Some researchers visualize the estimated displacement and strain fields following the path in;⁹ they focus on the Forward Problem. Some others, calculate from the displacement and strain fields, mechanical properties of the tissue such as Young's modulus, by using the constitutive elasticity equations solving the so called Inverse Problem. In the former, either axial strain or lateral strain,⁹ Poisson's ratio,¹⁴ or shear strain¹⁵ elastograms are visualized. The Inverse Problem approach, deals with Young's modulus visualization, the shear modulus¹⁶ or other related parameters. A comparative study between this two approaches can be found in.¹⁶

Email: dario@ctm.ulpgc.es, {marf,esuarz,jruiz}@itccanarias.org

Although elastography has been shown to be capable of detecting breast tumors in vivo,¹ biopsies are still needed to assess their malignancy. Malignant tumors are known to form ramified boundaries that become firmly bound to the surrounding tissue, as opposed to the benign ones, which have smooth borders and are loosely attached to its surrounding.¹ and¹⁵ have made efforts trying to reduce the use of biopsies, with US elastography.

In this paper we present the theory and procedure to assess the rotation of the tumor by visualizing the vorticity image aided with the strain tensor field as an effort to better determine the tumor infiltration, supported with a phantom study. Preliminary promising results show the potential of the technique in the diagnosis and prognosis of tumors, by non-invasively detecting their infiltrating nature.

This work is organized as follows. In Section 2, we present the mathematical basis from where we obtain the new parameters that we will use for visualization. We expose in Section 3 the motivation and preliminary investigations that made us deepen in this research. Section 4 presents the set up of the synthetic experiments and their results, discussing the visualization methods. Finally, in Section 5 the conclusions are related and the future work is also outlined.

2. MATHEMATICS: STRAIN AND DEFORMATION

Let $\mathbf{u} = (u_x, u_y)$ be a 2-D displacement vector field.¹⁷ In mechanical engineering is well known that the *displacement gradient matrix*, also known as *Jacobian matrix* or the *unit relative displacement matrix* (left of equation 1) can be decomposed into the strain tensor (the symmetric part) with the elongational strains on the diagonal and the shearing strains on the off-diagonal, and the vorticity tensor (the antisymmetric part) that contains only the vorticity components,¹⁷

$$\begin{bmatrix} \frac{\partial u_x}{\partial x} & \frac{\partial u_x}{\partial y} \\ \frac{\partial u_y}{\partial x} & \frac{\partial u_y}{\partial y} \end{bmatrix} = \begin{bmatrix} \frac{\partial u_x}{\partial x} & \frac{1}{2} \left(\frac{\partial u_x}{\partial y} + \frac{\partial u_y}{\partial x} \right) \\ \frac{1}{2} \left(\frac{\partial u_y}{\partial x} + \frac{\partial u_x}{\partial y} \right) & \frac{\partial u_y}{\partial y} \end{bmatrix} + \begin{bmatrix} 0 & \frac{1}{2} \left(\frac{\partial u_x}{\partial y} - \frac{\partial u_y}{\partial x} \right) \\ \frac{1}{2} \left(\frac{\partial u_y}{\partial x} - \frac{\partial u_x}{\partial y} \right) & 0 \end{bmatrix}. \quad (1)$$

For abbreviation we will represent this decomposition as $\nabla \mathbf{u} = \mathbf{E} + \mathbf{\Omega}$. The tensor \mathbf{E} measures the changes of shape locally (stretching or shortening), while $\mathbf{\Omega}$ informs about modifications related to rotations, and are defined by:

$$\mathbf{E} = \begin{bmatrix} \epsilon_x & \epsilon_{xy} \\ \epsilon_{yx} & \epsilon_y \end{bmatrix}, \text{ and } \mathbf{\Omega} = \begin{bmatrix} 0 & \omega_{xy} \\ \omega_{yx} & 0 \end{bmatrix}. \quad (2)$$

The columns in the strain matrix individually represent the unite relative displacement vectors, the first in the x -direction and the second in the y -direction, of two infinitesimal elements, each of one initially parallel to x -direction or to y -direction. From this, we can illustrate a physical interpretation of the shear components $\epsilon_{xy} = \epsilon_{yx}$. When there is no rotation, ϵ_{xy} is equal to the displacement in the y -direction of the two extremes of the infinitesimal element initially parallel to the x -direction divided by the length of that element. When there are both rotation and shear, the shear represents only part of the unit lateral relative displacement.

When the strain matrix components are zero, the local motion of the material in the neighborhood of a point is an infinitesimal rigid-body motion, through a small angle (compared to one radian). Vorticity can be extracted from this rotation tensor and is related to the amount of circulation or rotation. More strictly, the local angular rate of rotation. There are two conventions that differ by a factor of $\frac{1}{2}$ that affect the visualization of vorticity only in the scale of representation. We have followed the one related in¹⁸ where:

$$\frac{1}{2} \omega_z = \omega_{xy} = -\omega_{yx}. \quad (3)$$

3. TENSOR APPROACH TO ELASTOGRAPHY: MOTIVATION

Experiments done through simulations made us observe what intuitively could be expected from an unbounded inclusion inside an homogeneous background axially compressed with non symmetric boundary conditions. As it can be seen in figure 1 the inclusion rotates, and this doesn't happen with perfectly symmetric boundary conditions. This simulation solve the problem with FEA, but the analysis currently used in elastography cannot appreciate that rotation in a displacement image due to the limitation of the algorithms to detect small displacements. However parameters such as vorticity can give information about the differential rotation in the areas or volumes of study.

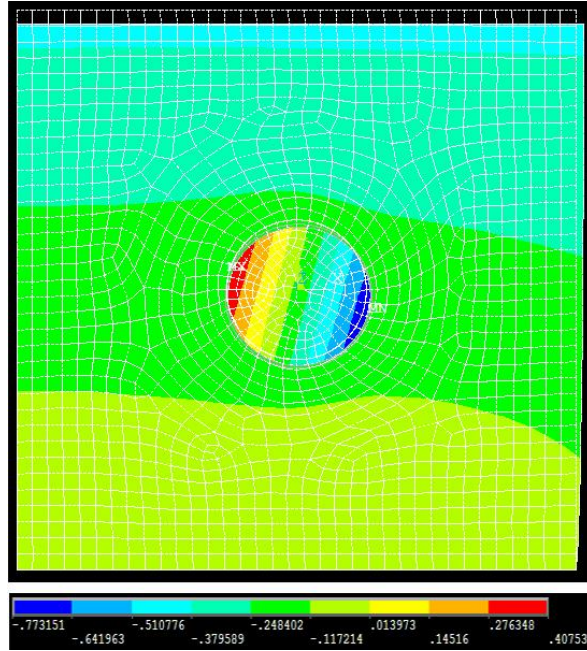


Figure 1. Axial displacement image corresponding to an unbounded inclusion 3 times stiffer than the background with non symmetric boundary conditions.

Opposed to how we calculate the strain tensor from the *displacement gradient matrix* (the *Jacobian*), the usual approach of elastography to the strain is to compute the formulas of each component of the strain tensor, therefore ignoring meaningful parameters as vorticity. As it was mentioned in section 1, most representations for elasticity imaging are scalar parameters, components of the strain tensor. Besides, tumor characterization haven't been solved. With the same goals but different means than other investigations such as¹ which utilizes the discrepancy in sonograms and elastograms, and¹⁵ through the shear strain visualization, we propose the study and analysis of the deformation tensor, and therefore, the strain tensor and the vorticity to asses tumor infiltration.

A main contribution of this paper is the hypothesis of infiltrating tumors being less prone to rotate than non-infiltrating ones when the surrounding tissue is pressed, since the former are more tightly attached to the normal tissue than the latter. Hence, we expect the vorticity to be zero at the background and non zero values for the infiltrating tumors, not as with non-infiltrating ones which should have also values around zero. We also expect the strain tensor to behave differently for this two cases, especially at the boundaries of the tumor. This difference can be assessed in the visualizations as we show next.

4. EXPERIMENTAL RESULTS

We have devised an experimental setting that has proved to be very useful in order to obtain preliminary results, prior to a clinical experimentation. The setting consists of a synthesis stage, where a digital phantom of the

tumor anatomy with surrounding tissue, the effect of the compression applied with the US probe, and the US images, are simulated. This setting allows us to easily experiment under different conditions and mechanical characteristics that we expect to correlate with real clinical data. The analysis stage estimates the deformation and elastic properties from the US data, and provides useful visualizations.

4.1. Synthesis

Tumors can be simulated digitally¹⁹ by a homogeneous background (the surrounding normal tissue), and a centered circular inclusion (the tumor) using finite element analysis (FEA) software. Mechanical properties are endowed to both the background and the inclusion. The level of infiltration is simulated by defining contact points and assigning to them a friction coefficient. For the specific setting reported in this paper the mechanical properties are as follows: for both inclusion and background, the Poisson's ratio used was $\mu = 0.495$,⁵ thus assuming conditions of virtual incompressibility. The background has a modulus of 21 kPa,⁵ and the inclusion was 3 times stiffer.

The FE models were generated with applications to elastography in mind with an area of $40 \times 40 \text{ mm}^2$ for the background, and 5 mm radius for the circular inclusion. The phantom was meshed using eight noded quadrilateral elements. Two different cases of boundary condition between the inclusion and the surrounding were studied: one of them with the inclusion loosely bounded to the background and the other fully connected, simulating the benign and malign tumors. We have been carrying out extensive experiments, with different mechanical properties and geometries in order to simulate many real situations, which we cannot report in this paper due to space limitations.

A compression was applied to the entire top side of the digital phantom, being 1% of its height. The top surface allow perfect slip conditions, but the bottom surface has movement restriction in both directions (axial and lateral). The sides of the target are free to move.

The coordinates of the nodes corresponding to the meshes of the test object before and after the compression are the outputs from the FEA program, and are considered as ground-truth data. These two sets of (x, y) coordinates were then computed with ultrasound simulation codes obtaining 15 frames of each, containing the RF A-lines for the Region of Interest (ROI). Comparing each pair of frames (pre and post) we estimated 15 displacement fields for our phantom. Averaging them all we produce elastograms as in the usual scalar way of visualization (top of figure 2). The parameters used for the simulation have been chosen according to our ultrasound equipment in order to validate the results in later works. Data were digitized at 40 MHz; 256 A-lines with a beam width of 1 mm, and the SNRs 170 dB. The pitch of the probe is 0.39 mm and its center frequency 7.5 MHz.

4.2. Analysis

Several techniques have been proposed to estimate the tensor strain components (section 1). All of them estimate a displacement vector field due to an applied deformation load. In this paper, we are not discussing which one is better, but how we can obtain more useful information from the displacement vector field. We computed the cross-correlation of the pre and post-compression RF A-lines, using 2 mm of window length and 80% of overlapping in order to obtain the displacement field. Further information on this issue can be found in.^{12,20} From the estimated displacement field we create its correspondent vector field. The gradient is calculated as in equation 1, after which we decompose it in the strain and the vorticity tensor fields.

4.3. Visualization

When visualizing the vorticity, we have represented the scalar value of:

$$\omega_z = 2 \cdot \omega_{xy} = -2 \cdot \omega_{yx} , \quad (4)$$

which represent the infinitesimal angle of the pure rotation experimented locally (considering the movement a compound of elongational terms and rotational ones, as seen in section 2, equation 3).

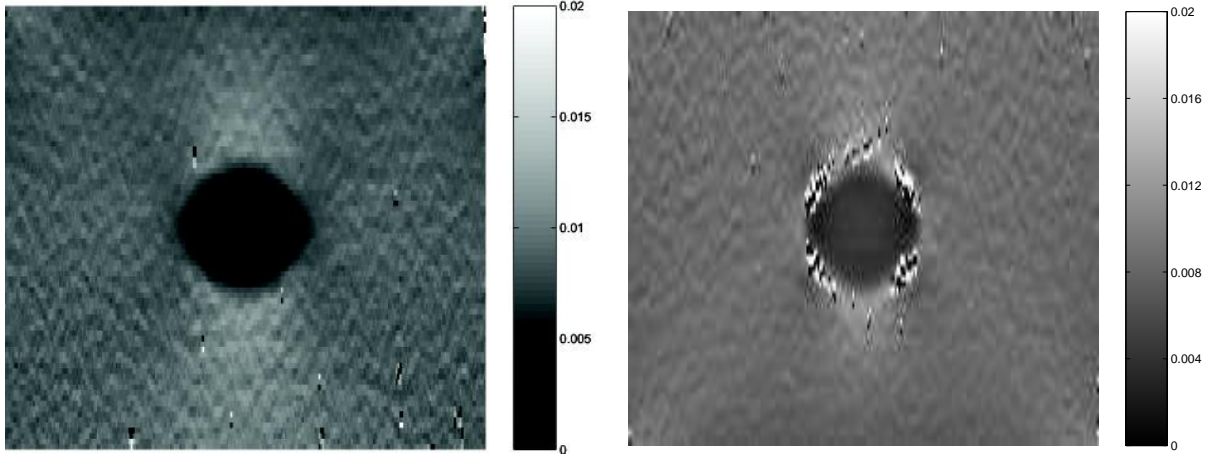


Figure 2. Scalar and tensorial images comparison. *Top:* axial elastograms; *bottom:* tensor elastograms. *Left:* bounded case (malign); *right:* unbounded case (benign).

5. DISCUSSION

The decomposition of the *displacement gradient matrix* in the strain tensor and the vorticity yields to the tensor visualization of the first and the scalar representation of the second. Here we are discussing only the second. The experiments presented in this paper show an homogeneous axially compressed target with symmetrical boundary conditions. Non-symmetric boundary conditions may be aided by the tensorial approach and vorticity visualization presented in this paper. Many applications in different elastographic modalities such as prostate elastography may be favored by the vorticity visualization and the tensorial approach presented here.

Although there are studies^{1,15} showing differences between malignant and benign tumors appreciated in axial strain and shear strain elastograms, the vorticity isolates the information about rotation in the deformation tensor and might contribute in the diagnosis and prognosis of in-vivo cancers (i.e. breast and prostate), what haven't been assessed, as far as we know, in other studies in elastography.

5.1. Real and estimated vorticity

In figure 3, we have included a representation of the ideal vorticity, meaning that we have computed the output of the FEA software without simulating the ultrasound. This image shows a ring similar to those found in shear elastograms,^{15,21} presenting too, diagonal symmetry. In our case black or white represent clockwise or anti-clockwise rotation. These effect is due to the behavior of the material around the inclusion. As the background absorbs more relative displacement when compressed (softer material), it seems intuitive to consider that it will sleep around the inclusion; clockwise at the right and anti-clockwise at the left, as if the inclusion would stay at the same position. However at the lower part of the inclusion the rotation is opposed to the former. Poisson's effect describes the lateral displacements due to the axial deformation. For this case of symmetric boundary conditions, the lateral stretching of the background to both sides of the target with no deformation of the inclusion, makes it easy to understand the direction of the rotations as they appear in the image 4.

The vorticity image of the US simulated response of the phantom yields a similar result, this time with the inherent noise of the US. Diagonal symmetry can also be appreciated, the direction of the rotation can be assessed with predominant positives or negatives values in each quadrant of the ring at the boundary of the inclusion.

5.2. Effect of boundary conditions

As related in section 3, part of this research was motivated for the results in the displacement images such as figure 1, with non-symmetric boundary conditions, which make the inclusion rotate when it is not bounded to the background. When these boundary conditions are symmetric, in theory, the inclusion would not rotate due to

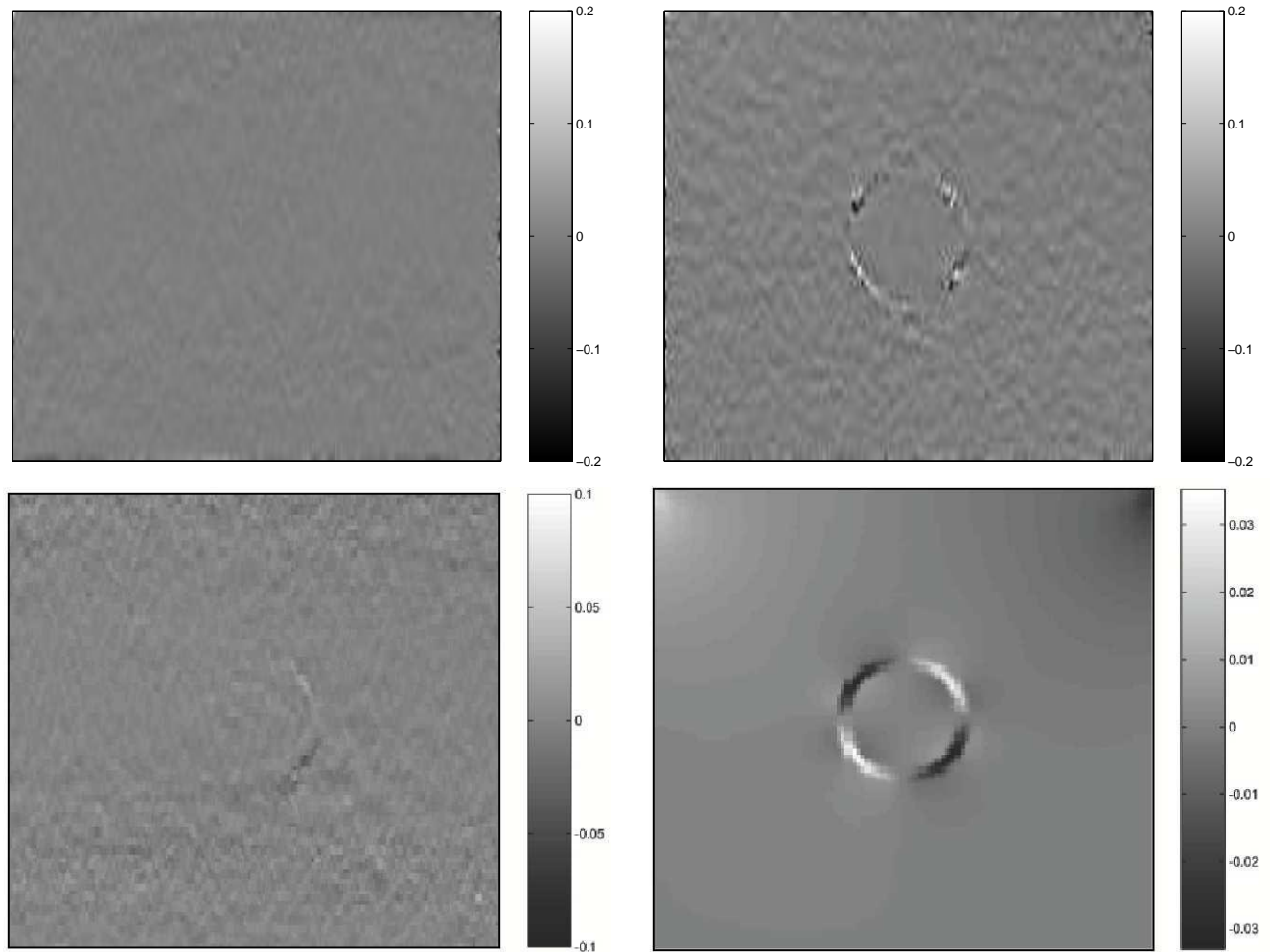


Figure 3. Vorticity images. *Top*: both with symmetric boundary conditions as described in the experimental set-up. *Left*: bounded case (malign); *right*: unbounded case (benign). For the bounded case the vorticity is homogeneous (for both the inclusion and the background), and for the unbounded case, one may observe the ring that appears too for the axial or the shear strain images, but this time isolated from the rest of the parameters. *Bottom*: *Left*: unbounded case with non-symmetric boundary conditions; *right*: ideal image for the unbounded case with symmetric boundary conditions.

the lateral equilibrium of the force system. However vorticity keeps showing information, due to its infinitesimal considerations exposed in section 2.

Comparing figures 3 *top right* and *bottom left*, we can explain how the boundary conditions affect the vorticity images and other elastographic representations. The former figure has symmetric boundary conditions, being the target free to move in both laterals. Instead, at the latter image, at the left side of the target we have imposed lateral movement equal to zero. The applied compression is pure axial and symmetric, but this time, as the target cannot stretch to the left, the whole lateral deformation takes place in direction to the other lateral. This yields as it can be seen in figure 3 *bottom left* to higher values of vorticity at the right of the inclusion, disappearing the diagonal symmetry encountered in the former image.

5.3. Effect of noise

We have introduced in the phantom study the effect of the noise produced by the acquisition equipment. The figures presented are the output of the simulated US response of the target after being processed with the

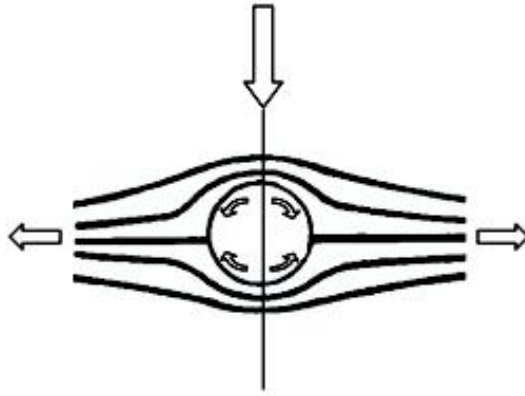


Figure 4. Rotation scheme. The circle represents the inclusion, and the lines are analogous to a flow, in our case the stretching of the background due to Poisson’s effect. The rows inside the circle show the directions of the background’s rotation with respect to the inclusion.

elastography algorithm. Although the input of the experiments are the ideal local positions of the phantom before and after the compression, the simulation experiment yields imperfect data closer to the expected real data. The effect of the noise was added to the US simulation code as a randomly chosen parameter in the range of 5% of relative error. Results are accurate enough to detect variations in the tensor representation as well as in vorticity, when the contrast ratio (equation 5) between the inclusion and the background is 3 or bigger. The effect of the contrast ratio is discussed in the next point. In-vivo elastograms are expected to behave similar to these presented here regarding to noise. Studies about the influence of the noise in the detectability of lesions using elastography can be found in.²²

$$\begin{aligned}
 \text{Contrast Ratio} = & \\
 & \frac{\text{Elastic Modulus of the Inclusion}}{\text{Elastic Modulus of the Background}} \tag{5}
 \end{aligned}$$

5.4. Effect of contrast ratio

We have repeated the experiment for three different contrast ratios: 1.25, 2 and 3. The bounded case has no difference for the three cases, and the visualization result is that shown in figure 3 right; an homogeneous image. In figure 5 it can be noticed that vorticity images with a contrast ratio lower than 3, are much noisier, making it difficult to distinguish between different rotational behaviors. However, as we present in figure 7, vorticity has higher values at the boundary of the unbounded inclusion for the three contrast ratios. This figure shows the statistical values of the vorticity in one representative column of the image matrix, the same for the three cases, where the inclusion is found and vorticity holds higher values at the boundary of the inclusion. In the case where the inclusion is three times stiffer than the background, the deviation from the median, and therefore the difference with the background, is one order higher than in the other two cases. Appropriate processing of the image might yield to results where this parameter can asses rotations at the target.

6. CONCLUSION AND ON-GOING RESEARCH

Other works visualize scalar values such as axial strain, shear strain and Poisson’s ratio, and have shown the usefulness of the information contained in them to assess the mobility of the tumor and therefore its malignancy.^{1,15} Vorticity isolates the information about rotation in the deformation tensor and might also contribute to the diagnosis and prognosis of in-vivo cancers (i.e. breast and prostate), what haven’t been assessed, as far as we know, in other studies in elastography.

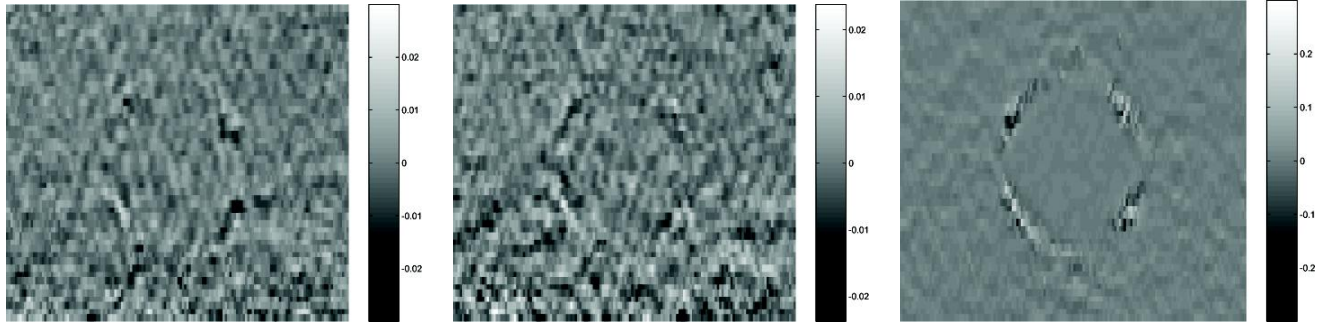


Figure 5. Vorticity images for different contrast ratios between the inclusion and the background. *Left*: contrast ratio of 1.25; *center*: contrast ratio of 2; *right*: contrast ratio of 3. Note the different scales of the images in order to better visualize each case.

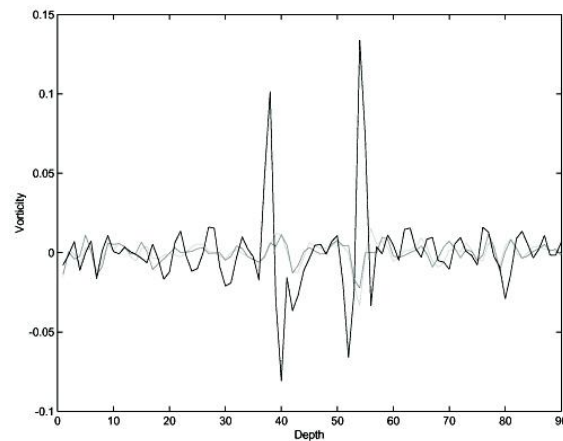


Figure 6. Vorticity against depth (in pixels) for the same representative column (passing through the inclusion at its right) for the 3 different contrast ratios between the inclusion and the background. *Light gray*: contrast ratio of 1.25; *gray*: contrast ratio of 2; *black*: contrast ratio of 3.

Our on-going research, deals with the use of new algorithms to estimate an accurate strain and vorticity tensor fields. Commercial and gelatin phantoms, and clinical validation are under study, as well as other tensorial data representations that can be extracted from the mathematical approach presented here.

Acknowledgments. Funding was provided by the Spanish Ministry of Science and Technology (TEC-2004-06647-C03-02), the European NoE SIMILAR FP6-507609 and for the second and third author, cofunded by MEC and Social European Funds, (*Torres Quevedo* PTQ2004-1443 and PTQ2004-1444, respectively). Thanks to C. Castaño-Moraga for his help.

REFERENCES

1. B. Garra, I. Céspedes, J. Ophir, S. Spratt, R. A. Zuurbier, C. M. Magnant, and M. F. Pennanen, “Elastography of breast lesions: initial clinical results,” *Radiology* **202**, pp. 79–86, 1997.
2. K. M. Hiltawsky, M. Kruger, C. Starke, L. Heuser, H. Ermert, and A. Jensen, “Freehand ultrasound elastography of breast lesions: Clinical results,” *Ultrasound Med. Biol.* **27**, pp. 1461–1469, 2001.
3. M. Shling, M. Arigovindan, C. Jansen, P. Hunziker, and M. Unser, “Myocardial motion analysis from b-mode echocardiograms,” *IEEE Transactions on Image Processing* **14**, April 2005.

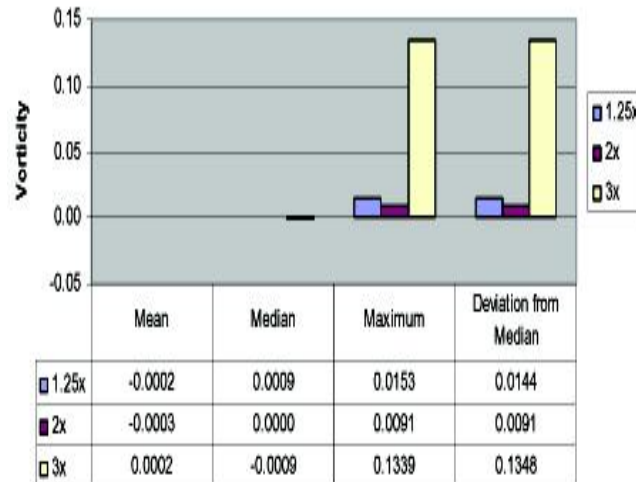


Figure 7. Vorticity’s mean, median, maximum value and deviation from the median for the 3 different contrast ratios between the inclusion and the background.

4. R. L. Maurice, M. Daronat, J. Ohayon, E. Stoyanova¹, F. S. Foster, and G. Cloutier, “Non-invasive high-frequency vascular ultrasound elastography,” *Phys. Med. Biol.* **50**, 16111628, 2005.
5. T. Krouskop, T. Wheeler, F. Kallel, B. Garra, and T. Hall, “Elastic moduli of breast and prostate tissue under compression,” *Ultrasonic Imaging* **20**, pp. 260–274, 1998.
6. S. Srinivasan, T. Krouskop, and J. Ophir, “Comparing elastographic strain images with modulus images obtained using nano-indentation: Preliminary results using phantoms and tissue samples,” *Ultrasound in Medicine and Biology* **30**(3), pp. 329–343, 2004.
7. D. Duncan and S. Kirkpatrick, “Processing algorithms for tracking speckle shifts in optical elastography of biological tissues,” *Journl of Biomedical Optics* **6**, pp. 418–426, July 2001.
8. K. J. Parker, L. S. Taylor, and S. Gracewski, “A unified view of imaging the elastic properties of tissue,” *Acoustical Society of America* **117**(5), pp. 2705–2712, 2005.
9. J. Ophir, I. Céspedes, B. Garra, H. Ponnekanti, Y. Huang, and N. Maklad, “Elastography: a quantitative method for imaging the elasticity of biological tissues,” 1991.
10. M. M. Doyley, J. C. Bamber, F. Fuechsel, and N. L. Bush, “A freehand elastographic imaging approach for clinical breast imaging: System development and performance evaluation,” *Ultrasound in Medicine and Biology* **27**, pp. 1347–1357, 2001.
11. T. Otake, T. Kawano, S. T. T. Mitake, and S. Umemura, “High-quality/high-resolution digital ultrasound diagnostic scanner,” *Hitachi Review* **52**(4), 2003.
12. S. Srinivasan, F. Kallel, R. Souchon, and J. Ophir, “Analysis of an adaptive strain estimation technique in elastography,” *Ultrasonic Imaging* **24**, pp. 109–118, 2002.
13. A. Pesavento, C. Perrey, M. Krueger, and H. Ermert, “A time-efficient and accurate strain estimation concept for ultrasonic elastography using iterative phase zero estimation,” *IEEE Transactions on Ultrasonics, Ferroelectrics, and Frequency Control* **46**, pp. 1057–1067, September 1999.
14. R. Righetti, J. Ophir, S. Srinivasan, and T. Krouskop, “The feasibility of using elastography for imaging the poisson’s ratio in porous media,” *Ultrasound in Medicine and Biology* **30**(2), pp. 215–228, 2004.
15. E. E. Konofagou, T. Harrigan, and J. Ophir, “Shear strain estimation and lesion mobility assessment in elastography,” *Ultrasonics* **38**, pp. 400–404, 2000.
16. M. Doyley, S. Srinivasan, S. Pendergrass, Z. Wu, and J. Ophir, “Comparative evaluation of strain-based and model-based modulus elastography,” *Ultrasound in Medicine and Biology* **31**(6), pp. 787–802, 2005.
17. L. Malvern, *Introduction to the Mechanics of a Continuous Medium*, Ed. Prentice Hall, 1969.

18. D. Tritton, *Physical Fluid Dynamics*, Oxford Science Publications, 1977.
19. D. Sosa-Cabrera, J. Ophir, T. Krouskop, A. T. Kumar, and J. Ruiz-Alzola, "Study of the effect of boundary conditions and inclusion's position on the contrast transfer efficiency in elastography," in *IV International Conference on the Ultrasonic Measurement and Imaging of Tissue Elasticity*, p. 94, October 2005.
20. E. E. Konofagou and O. J., "A new elastographic method for estimation and imaging of lateral displacements, lateral strains, corrected axial strains and poisson's ratios in tissues," *Ultrasound in Medicine and Biology* **24**(8), pp. 1183–1199, 1998.
21. U. Techavipoo, Q. Chen, T. Varghese, and J. A. Zagzebski, "Estimation of displacement vectors and strain tensors in elastography using angular insonifications," *IEEE Transactions on Medical Imaging* **23**, December 2004.
22. N. Belaid, I. Céspedes, J. Thijssen, and J. Ophir, "Lesion detection in simulated elastographic and ecographic images: A psycho-physical study," *Ultrasound in Medicine and Biology* **20**, pp. 877–891, 1994.